Including Finite Surface Span Effects in Empirical Jet-Surface Interaction Noise Models

Cliff Brown *

NASA Glenn Research Center, Cleveland, OH, 44135, USA

Far-field experimental noise data have been acquired for a simple single-stream round jet near a flat surface with finite span. These data have been used to build empirical models that describe the effect of finite surface span on the jet-surface interaction (JSI) noise source and on the shielding of the jet-mixing noise. These models have been integrated into existing JSI noise source and shielding effect models developed for infinite span surfaces. The finite span models work with the infinite span models to extend the prediction capability over a range of polar and azimuthal observer angles not covered in the original experiments. The development of the finite span models is described, with the underlying data, and the new models are combined with existing models to create an empirical exhaust noise prediction tool that supports finite surface span. Comparisons back to the underlying experimental data are used to verify that the models and codes are working as intended.

Nomenclature

$\gamma_{\theta 1,\theta 2}$	coherence between observers at angles θ_1 and θ_2
ϕ	observation angle relative to the zenith (azimuthal or roll angle)
ϕ_E	azimuthal angle from jet centerline to spanwise surface edge
θ	observation angle relative to the upstream jet axis (polar or yaw angle)
$C_{1,JSI}$	peak amplitude model in the jet-surface noise source model
$C_{1,S,\theta}$	model for linear term in shielding effect model
$C_{2,JSI}$	spectral width model in the jet-surface noise source model
$C_{2,S,\theta}$	model for constant term in shielding effect model
c_a	speed of sound at ambient conditions
$C_{span,JSI}$	model for the effect of finite span on the jet-surface interaction nose source
$C_{span,shield}$	model for the effect of finite span on the surface shielding effect
D_j	nozzle exit diameter
f	frequency
$F_{peak,JSI}$	peak frequency model in the jet-surface noise source model
G_S	surface shielding of jet mixing noise
h_E	radial distance from jet lipline to surface (in inches)
M_a	acoustic Mach number ($M_a = U_j/c_a$)
$OASPL_{FS}$	overall sound pressure level for finite span surface
$OASPL_{IS}$	overall sound pressure level for infinite span surface
P_a	ambient pressure
P_d	jet-surface interaction (dipole) noise
P_m	jet mixing noise
$P_{t,j}$	total jet pressure
PSD_T	power spectral density of combined sources and effects
St_{Dj}	Strouhal number ($St_{Dj} = fD_j/U_j$)
T_sR	jet static temperature ratio
T_tR	jet total temperature ratio

*Research Engineer, Acoustics Branch, 21000 Brookpark Rd., AIAA Member.

U_j	jet exit velocity
x_C	jet potential core length
x_E	axial distance from jet exit to surface trailing edge
y_E	surface span

I. Introduction

Empirical models are used in many situations to explore the behavior of complex systems. These models are created using experimental data from a similar system and provide predicted results for inputs between the data points. As a result, an empirical model relies on the detail and accuracy of the underlying data to define its range and applicability. For example, a model built on a highly detailed experimental data set will often provide a good prediction for that particular setup but will not be acceptable for a similar setup with one or two key changes. In contrast, a model created using a more generic experimental data base may have more uncertainty in any one case but provide useful guidance across a wider range of variables. This tradeoff can also allow models that are grown from simple to more complex cases as the underlying design is defined.

Jet exhaust noise has been a issue for communities near major airports since the advent of jet aircraft in the 1950's and while modern aircraft are much quieter today than in the past, noise remains an issue due in part to an large increase in the frequency of flights. Modern aircraft are also designed with the engines more tightly integrated with the airframe which increases operational efficiency. However, this integration may create a noise problem as the turbulent energy in the engine exhaust flow is scattered into acoustic energy when the turbulence travels over the surface edge; and while this jet-surface interaction (JSI) noise is often the dominant source at low frequencies,[1–4] the surface may also shield the jet mixing noise from people on the ground (or reflect it to increase the noise on the ground). This creates a complex system of trade-offs between noise sources in different portions of the spectra that must be considered in the aircraft design phase.

Jet noise prediction methods have become fairly reliable for isolated plumes but generally fail to capture the changes that occur when nearby surfaces are considered or require too much time and computational effort for use in system level studies where the major design trade-offs occur. Therefore, a set of empirical models have been built using a database acquired in a series of tests at the NASA Glenn Research Center.[3–5] These models[8,9] are based on experimental data acquired using a simple single-stream round nozzle near a semi-infinite flat plate. This generic configuration allows the model to provide guidance over a large range of more specific cases but with a higher level of uncertainty introduced by assumptions required to simplify the geometry. These assumptions can be reduced as data are acquired from configurations that incorporate new elements of realistic aircraft and are added into the existing empirical models. One such addition is the inclusion of finite surface spans.

Semi-infinite surfaces were used to greatly simplify the first series of JSI noise experiments and models; finite span surfaces introduce the potential for side edge effects and make azimuthal angle much more significant. In fact, azimuthal angle does not appear in the shielding model for infinite span surfaces where the observer is either entirely above or entirely below the surface regardless of angle. However, finite span surfaces are reality so efforts have been made to improve the existing JSI models by including the effect of finite span on the JSI noise source and on the shielding effect. A test program was conducted to acquire the far-field noise data using a range of surfaces with three microphones arrays (two in polar angle and one in azimuthal angle). The data have been used to develop models that give a correction to the semi-infinite span level.

II. Experimental Data

The complexity of a system may be represented by the number of independent variables. The current JSI noise database includes seven independent variables: jet operating condition (Mach number and temperature ratio), surface length and standoff distance, observer location (polar and azimuthal angles), and frequency. By assuming that the surface is semi-infinite (and ensuring that is the case using phased array data[3,5]), the experimental setup is simplified and the number of data points required is limited. To remove this assumption, a new experimental setup was required to accommodate a range of surface spans and simultaneously measure the far-field noise at multiple azimuthal angles.

II.A. Test Setup, Data Acquisition and Data Processing

The JSI experiments were conducted using the Small Hot Jet Acoustic Rig (SHJAR) located in the Aero-Acoustic Propulsion Laboratory at the NASA Glenn Research Center. The SHJAR is a capable of supplying a single-stream nozzle with up to 2.7 kg/s of air. A hydrogen burning combustor heats the air up to 975 K to simulate core exhaust temperatures. Flow conditioning and a line-of-sight muffler are used to provide clean flow with minimal rig noise at jet exit Mach numbers as low as $M_a = 0.35$. Additional information on the SHJAR and performance validation data can be found in [6, 7]. The AAPL is a geodesic dome covered by sound absorbing wedges to create an anechoic environment at frequencies above 200 Hz. A facility computer system monitors and records all relevant rig and atmospheric temperatures and pressures once per second. The desired jet exit conditions are entered into this system which then computes the difference between the current and requested flow; this difference must remain under 0.5% for the duration of the acquisition for a point to be accepted. The jet conditions tested are shown in Table 1.

The far-field noise data were simultaneously acquired using three microphone arrays (Figure 1). The first polar array contains 24 microphones at 5° increment ranging from $50° \leq \theta \leq 165°$ in a plane parallel to the floor. The second polar array, rotated in azimuthal angle by 90° from the first, contains 18 microphones at 5° increment ($80° \leq \theta \leq 165°$) because the SHJAR face blocks any microphones that might be farther upstream. An azimuthal array at $\theta = 90°$ containing 15 microphones at 10° increment from $0° \leq \phi \leq 150°$ was also deployed. All microphones were Bruel & Kjaer 1/4" type 4939. Bruel & Kjaer Nexus units provided the signal conditioning and amplification. The data were digitized and recorded by two DataMAX Instrumentation Recorders from R.C. Electronics synchronized so all points were acquired simultaneously for a 10 second sample time using a 200 kHz sample rate. Combined these arrays show the effect of finite span while minimizing the number of model rotations required. Note, however, that data were only acquired for the shielded observer (surface between the jet and microphone array).

A single-stream round nozzle ($D_j = 2$"), previously tested in isolated[6] and near a surface[3,4] was used for these tests. Surfaces tested were made using flat aluminum plates with a 45° beveled trailing edge to be consistent with earlier experiments.[3] An example surface is shown in Figure 2 with the nomenclature used to describe the surface dimensions and positions. The surface length (x_E), standoff distances (h_E), and span lengths (y_E) tested are given in Table 2.

Once acquired, the time series data were transformed to the frequency domain using a standard fast Fourier transform routine with a 2^{14} point Kaiser window giving a spectral resolution of 12.21 Hz. The background noise, recorded at the beginning of each run, was then subtracted on a frequency by frequency basis; any frequency where the measured data was within 3 dB of the background noise was removed to minimize contamination the the database. The data were corrected for the frequency response of each individual microphone using the calibration supplied by the manufacturer, corrected for atmospheric attenuation to a lossless condition, and scaled to arc distance of $100D_j$.

Setpoint	NPR $P_{t,j}/P_a$	T_tR $T_{t,j}/T_a$	T_sR $T_{s,j}/T_a$	M_a U_j/c_a
3	1.197	1.0	0.968	0.5
5	1.436	1.0	0.902	0.7
7	1.860	1.0	0.835	0.9

Table 1. Unheated subsonic jet exit conditions common to all the jet-surface interaction noise tests.

II.B. Spectral Separation

The measured spectra contains the jet-mixing noise, JSI noise, and the shielding of the jet-mixing noise by the surface. The empirical models, however, address each of these components separately and, therefore, additional processing is required to separate the measured spectra before the models can be developed. The spectral separation method used requires two independent measurements: the jet-mixing noise (P_m), measured by removing the surface and running the same jet conditions, and the total noise (PSD_T) of the system with the surface in place. The post-processing of these data to separate the individual sources, which was previously used to develop the infinite span models, is briefly described here and additional details can be found in [9] and [12].

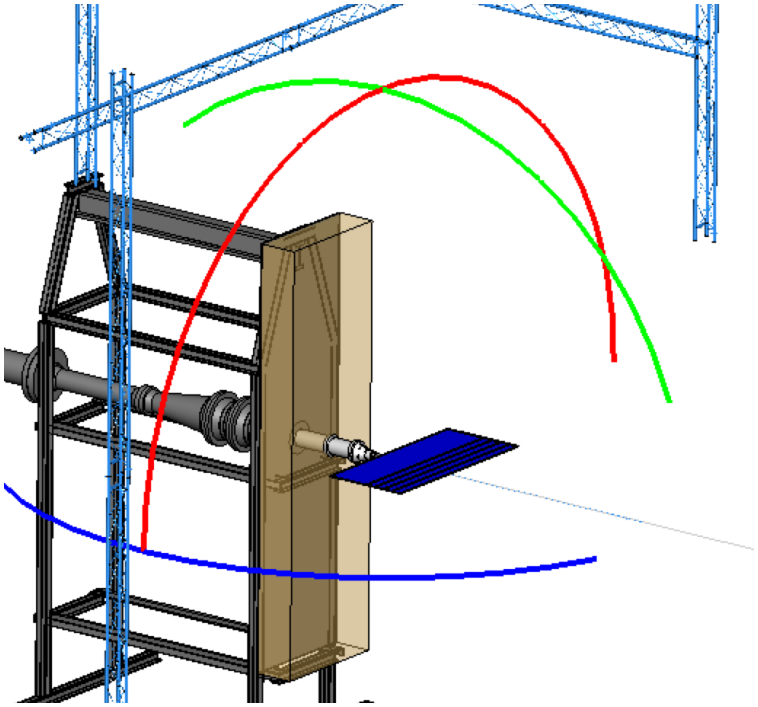

Figure 1. Schematic showing the SHJAR with a surface and the three microphone arrays used to acquire the far-field noise data. The two polar arrays are located at $\phi = 0^\circ$ (green) and $\phi = 90^\circ$ (blue). The azimuthal array is located at $\theta = 90^\circ$ (red).

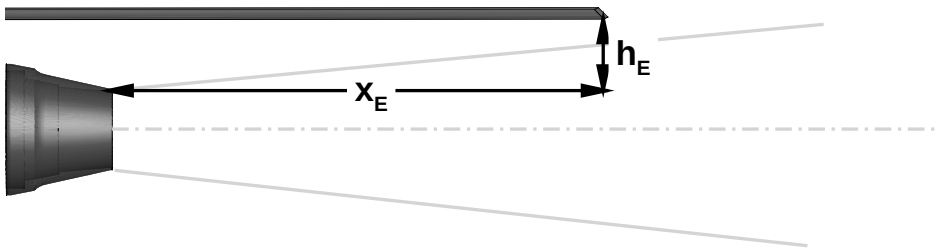

(a) Side View

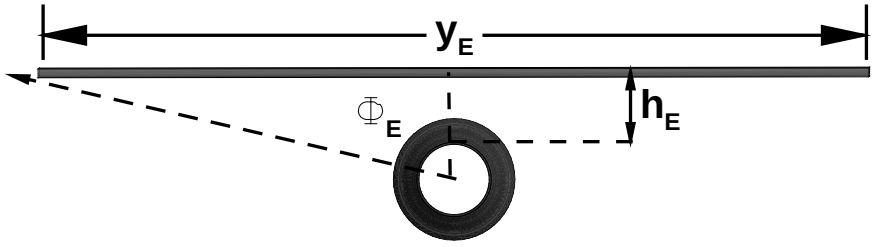

(b) Front View

Figure 2. Schematic showing the configuration tested with the nomenclature used to describe the surface locations.

h_E (inches)	x_E (inches)				
	1.3	2.7	4	8	12
0.0	24	24	24,12,6,4,2,1	24	24,12,6,4,2,1
0.1	24	24	24,12,6,4,2,1	24	24,12,6,4,2,1
0.2	24	24	24,12,6,4,2,1	24	24,12,6,4,2,1
0.3	24	24	24,12,6,4,2,1	24	24,12,6,4,2,1
0.5	24	24	24,12,6,4,2,1	24	24,12,6,4,2,1
0.7	24	24	24,12,6,4,2,1	24	24,12,6,4,2,1
1.0	24	24	24,12,6,4,2,1	24	24,12,6,4,2,1
1.4	24	24	24,12,6,4,2,1	24	24,12,6,4,2,1
1.9	24	24	24,12,6,4,2,1	24	24,12,6,4,2,1
2.5	24	24	24,12,6,4,2,1	24	24,12,6,4,2,1
3.2	24	24	24,12,6,4,2,1	24	24,12,6,4,2,1
4.0	24	24	24,12,6,4,2,1	24	24,12,6,4,2,1
5.0	24	24	24,12,6,4,2,1	24	24,12,6,4,2,1

Table 2. Surface lengths (x_E) and radial distances (h_E) acquired during experiments as the basis for the empirical model. The numbers in each box are the surface span lengths (y_E) in inches.

Experimental data have shown that the JSI noise source (P_d) is dipolar and, therefore, coherent across a wide range of observer angles.[3] The jet-mixing noise source, however, is characterized as a distribution of incoherent sources and, in practice, coherent over a small range of angles. These properties allow P_d to be extracted from PSD_T; the coherent part of the spectra belongs to P_d. Mathematically, this operation appears as:

$$P_d = PSD_T * \gamma_{\theta 1,\theta 2} \tag{1}$$

where $\gamma_{\theta 1,\theta 2}$ is the coherence between two observers approximately 30° apart. Figure 3 shows an example of this process for an ideal configuration: low jet Mach number (setpoint 3) with a longer surface ($x_E = 12$, and short standoff distance ($h_E = 0.5$). The coherence (Figure 3(a)) of PSD_T is much higher than P_m over the range of frequencies corresponding to increase in noise above P_m and this increase is attributed to P_d, the JSI noise source.

The jet-mixing noise shielding effect (G_S) can be determined once PSD_T, P_m, and P_d are known. In this method, spectral characteristics not captured by a noise source included in G_S so that:

$$G_S = \left(PSD_T \ominus P_d\right) - P_m \tag{2}$$

where $\ominus$ indicates spectral subtraction based on power (anti-logarithmically) and $-$ indicates subtraction of dB values. Note that Equation 2 contains two spectral subtractions making the result prone to fluctuations due to small variations in PSD_T, P_m, and $\gamma_{\theta 1,\theta 2}$. A sample shielding effect spectra is shown in Figure 3(c) where the imperfect coherence (maximum $\gamma_{\theta 1,\theta 2} \approx 0.95$) leads to a nonzero result at frequencies below $St_{Dj} \leq 1$. The lowest shielded frequencies in this case appear to be around $St_{Dj} = 1$, however, it is often difficult find the exact frequency where $G_S = 0$. At higher frequencies, the shielding effect is relatively smooth and increasing (indicated by larger magnitude negative numbers).

The example shown in Figure 3 is a good case for source separation. The amplitude of P_d to P_m is higher when the surface is close to the jet ($h_E = 0.5$ in this case) and when the jet Mach number is lower, in this case $M_a = 0.5$, improving the results (P_d is dipolar so it scales as U_j^6 while P_m scales as U_j^8). Additionally, the shielding is improved when the surface in longer ($x_E = 12$ in this case) so small variations in level are an even smaller percentage of the effect. Therefore, it is important to remember that not all cases will result in a clean spectral separation. Furthermore, small variations in level between configurations can result in inconsistent behavior, on the order of 1 dB, when those cases are compared later (e.g. a case that should have slightly more shielded does not because the jet velocity was slightly higher). The impact of these discrepancies may be reduced by using many cases to when fitting the models to the data.

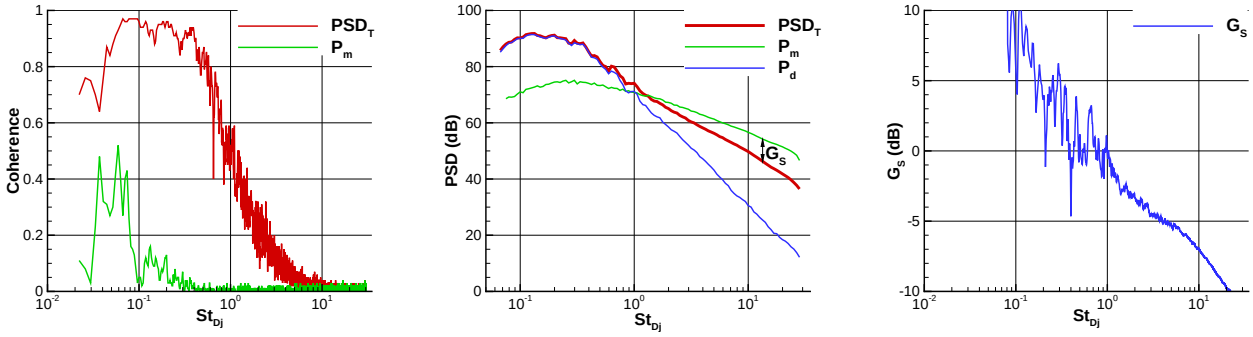

(a) Coherence (b) Spectra (c) Shielding

Figure 3. An example of separating the JSI spectra (P_d) and surface shielding effect (G_S) from the measured jet-mixing noise (P_m) at setpoint 3 and noise measured at setpoint 3 with a surface at $x_E = 12$, $h_E = 0.5$ (PSD_T).

III. Empirical Models

III.A. Infinite Span Models

The finite span models provide a correction to the results predicted by the existing infinite span models. It is, therefore, necessary to understand how these existing models function in order to ensure that the new models are compatible. The equation to predict the combined spectra for all sources and effects (PSD_T) for a round jet near a semi-infinite shielding surface is:

$$PSD_T = (P_m + G_S) \oplus P_d \tag{3}$$

where P_m represents the jet-mixing noise source, G_S represents the surface shielding effect, P_d represents the JSI noise source. Note that + indicates an effect is added logarithmically (dB values) and $\oplus$ indicates sources summed in acoustic power (anti-logarithmically). The framework described by Equation 3 combines separate models for each source and effect to create a modular prediction methodology. An existing empirical model for the jet-mixing noise source (P_m)[10,11] does not, by definition, depend on any surface variables but the infinite span models for P_d and G_S must be modified to account for surface span as well as surface length and standoff distance.

A JSI noise source model (P_d) has been previously developed for infinite span surfaces. Experimental data has shown that P_d for these configurations is dominated by the trailing edge 'scattering' source which is dipolar in nature. The JSI noise source model takes advantage of this by predicting a characteristic spectra, defined at $\theta = 90°$, $\phi = 0°$, and then using the established directivity of dipole sources to project that spectra to other observer angles. Mathematically, P_d in Equation 3 can be expanded as:

$$P_d = \left[C_{1,JSI} + C_{2,JSI}\, log_{10}(f/F_{peak,JSI})^2\right]\left[sin(\theta)\, cos(\phi)\right] \tag{4}$$

where $C_{1,JSI}$ sets the peak amplitude, $C_{2,JSI}$ gives the spectra width, $F_{peak,JSI}$ sets the frequency of the spectral peak, and the term $sin(\theta)\, cos(\phi)$ imposes the dipole directivity. The coefficients $C_{1,JSI}$, $C_{2,JSI}$, and $F_{peak,JSI}$ are each functions of surface position (x_E and h_E) and jet exit conditions (M_a and T_tR) [a] and represent the underlying empirical models used to predict $P_d(x_E, h_E, M_a, T_{t,j}, f, \theta, \phi)$.

A model for the shielding of jet mixing noise, G_S, by an infinite span surface has also been developed previously.[9] This is a logarithmic model using the equation:

$$G_S = C_{1,S,\theta}\, log_{10}(St_{Dj}) + C_{2,S,\theta} \tag{5}$$

where $C_{1,S,\theta}$ gives the rate of change with frequency and $C_{2,S,\theta}$ shifts the minimum frequency where the shielding effect begins. Similar to the JSI source model, $C_{1,S,\theta}$ and $C_{2,S,\theta}$ represent the underlying empirical

[a]These models use jet potential core length (X_c) to nondimensionalize surface length so additional flow variables, commonly static temperature ratio, may also appear depending on the model used to estimate the jet potential core length.

models and are functions of surface position (x_E and h_E) and the jet exit condition (introduced though a potential core length model). However, unlike the JSI source model the shielding model uses different set of coefficients for each polar angle in the dataset and then interpolates for intermediate angles. The shielding models are bilinear in nondimensional surface position and can be written as:

$$C_{1,S,\theta}(x_E/x_C, h_E/x_E) = K_{1,S,\theta} + K_{2,S,\theta}(x_E/x_C) + K_{3,S,\theta}(h_E/x_E) \quad (6)$$

$$C_{2,S,\theta}(x_E/x_C, h_E/x_E) = K_{4,S,\theta} + K_{5,S,\theta}(x_E/x_C) + K_{6,S,\theta}(h_E/x_E) \quad (7)$$

where $K_{1-6,S\theta}$ are model coefficients and x_C is the jet potential core length. Since x_C depends on the jet exit conditions, the function form of the shielding effect model can be expressed as $G_S(x_E, h_E, M_a, T_sR, f, \theta)$. Note that the observer azimuthal angle ϕ does not appear in the list of independent variables; the observer is either on the shielded ($\phi = 0°$) or reflected ($\phi = 180°$) if the surface has infinite span.

III.B. Finite Span Model for JSI Source

The semi-infinite span empirical model that gives the JSI noise source spectra is based on a dataset with significant variations in surface length (x_E), standoff distance (h_E) and jet flow conditions (M_a and TTR); adding surface span as another independent variable would require an unreasonable amount of test time. Therefore, only a subset of surface lengths and jet conditions were tested with all the surface spans limiting the number of data points available to develop the finite span model and requiring a method of extending the model to cover the full range supported by the original infinite surface span model be integrated into the model.

The JSI noise spectra (P_d) in the configurations tested is dominated by the scattering source at the trailing edge[3,5] and, therefore, is expected to scale with the length of edge that experiences flow. A natural break might also be expected at the span length where the jet spreads past the spanwise edge reducing the length available to the trailing edge source and introducing the possibility for additional sources on the spanwise edges. Figure 4 shows the JSI characteristic spectra (P_d at $\theta = 90°$, $\phi = 0°$) for all surface and span lengths tested at setpoint 3; the span length has been nondimensionalized by the surface length to account for the amount of jet spread at the trailing edge. While the spectral shape is different between $x_E = 4$ (Figure 4(a)) and $x_E = 12$ (Figure 4(b)), the trend with increasing span is consistent. First, the major feature is an increase in amplitude ($C_{1,JSI}$ in Equation 4) as span increases up to approximately $y_E/x_E = 1$ where the it reaches the level of the infinite span spectra. Second, the spectral width ($C_{2,JSI}$ in Equation 4) increases, primarily on the low frequency side of the spectra, as the span length increases. The underlying model for the JSI noise source (P_d) assumes a symmetric parabolic spectral profile so a change to capture this effect in the P_d model will require a significant modification. Finally, there is a shift in the frequency corresponding to the peak amplitude ($F_{peak,JSI}$ in Equation 4) that appears primarily in the $x_E = 12$ data (possibly because of the finer resolution in y_E/x_E at $x_E = 12$). The shift appears as a discontinuity in this data set, occurring between $0.5 \leq y_E/x_E \leq 1.0$, and, therefore, is difficult to capture in a simple model. Overall, these data show that the first-order effect of finite span is a change in amplitude. The spectral width and frequency corresponding to the peak amplitude also change but these are smaller changes and more difficult to capture in a simple model. The initial modeling effort, therefore, will focus on capturing the change in amplitude.

The finite span model must (1) capture the change in amplitude that occurs with a change in span and (2) extend over the range of surface configurations supported by the underlying infinite span model. To accomplish these goals, the OASPL of the JSI noise spectra was computed from the finite span data ($OASPL_{FS}$) and then normalized by the OASPL for the corresponding infinite span ($OASPL_{IS}$) to give a percentage change of the overall level associated with each span length. The results, shown in Figure 5, provide some insight into how span length effects the JSI noise. First, these normalized data show that the span effect reduces the amplitude by approximately 15% from the semi-infinite span to the narrowest span tested; this represents the maximum range of the effect. Second, a rapid change occurs over $0.083 \leq y_E/x_E \leq 1$ and then hovers around 1 for $y_E/x_E > 1$ with a small ($\approx 1\%$) overshoot between $1 \leq y_E/x_E \leq 2$. A logarithmic function seems appropriate to capture this behavior. The normalized values $OASPL_{FS}/OASPL_{IS}$, as functions of $log_{10}(y_E/x_E)$, are shown for various jet conditions in Figure 5(a) and for different surface standoff distances (h_E) in Figure 5(b) standoff distances; the agreement between these lines shows that this behavior is relatively robust.

The finite span model modifies the characteristic spectra ($P_d(\theta = 90°, \phi = 0°)$ produced by the infinite span model and then uses the directivity defined by the infinite span model to propagate those changes other observer locations. Mathematically, the finite span model modifies the amplitude term ($C_{1,JSI}$ in Equation 4) in the JSI source model to give P_d for a finite span as:

$$P_d = \left[C_{1,JSI} * \mathbf{C_{span,JSI}} + C_{2,JSI}\, log_{10}(f/F_{peak,JSI})^2\right]\left[sin(\theta)\, cos(\phi)\right] \tag{8}$$

where $C_{span,JSI}$ represents the finite span model which returns the $OASPL_{FS}/OASPL_{IS}$ ratio. This implementation the advantage of setting built-in limits on the finite span model; it cannot give a value greater than one (infinite span) or less than zero (theoretical zero span).

The empirical finite span effect model was formed using a least-squares fit to the $OASPL_{FS}/OASPL_{IS}$ ratio computed for all spans, surface standoff distances, and jet conditions tested. The fit equation was quadratic with $log_{10}(y_E/x_E)$ as the independent variable. The model for the effect of surface span on the JSI noise source is:

$$C_{span,JSI} = -0.0691 * [log_{10}(y_E/x_E)]^2 + 0.0707 * log_{10}(y_E/x_E) + 0.9906 \tag{9}$$

where $C_{span,JSI}$ is the ratio $OASPL_{FS}/OASPL_{IS}$. Figure 6 shows the $OASPL_{FS}/OASPL_{IS}$ experimental data plotted with the corresponding model results.

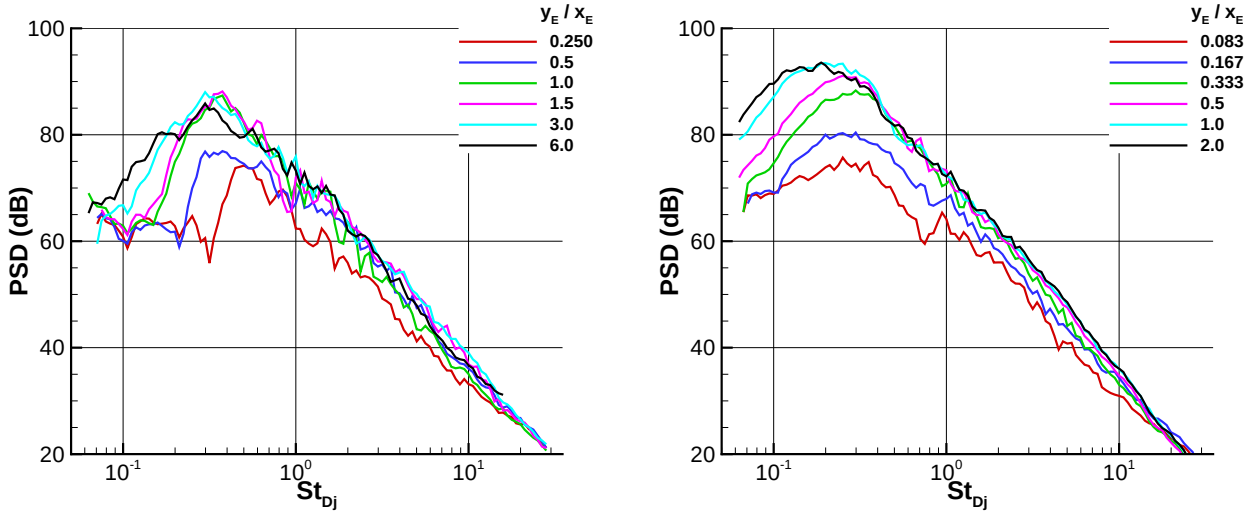

(a) $x_E = 4$ (b) $x_E = 12$

Figure 4. Extracted JSI noise source spectra (P_d) for all surface spans (y_E/x_E) acquired at $\theta = 90°$, $\phi = 0°$, setpoint 3, and $hE = 0$.

III.C. Finite Span Model for Shielding of Jet Mixing Noise

The empirical for the shielding of jet mixing noise by an infinite span surface computes reduction, in dB, as a function of surface length, standoff distance, jet conditions (via jet potential core length), and observer polar angle. The observer azimuthal angle does not enter the model because the observer is either shielded or not shielded when the span is infinite; azimuthal angle must only be included in the model when the span is finite. The azimuthal array in the experiments was located at $\theta = 90°$ but the model must extend across all polar angles so, like the JSI source model, the finite span model must incorporate a method to extend the results across the full range supported by the infinite span model.

The shielding effect is the result of two spectral subtractions and is often relatively small in magnitude. It is, therefore, subject to more variability than the JSI or jet mixing noise sources (as discussed in Section II.B). Figure 7 shows shielding effect spectra for two azimuthal angles and two surface lengths. At $x_E = 12$, for example, the shielding effect is approximately 5 dB at $St_{Dj} = 10$; a 1 dB uncertainty between two independent measurements (with and without the surface) results in a 20% variation in the shielding effect

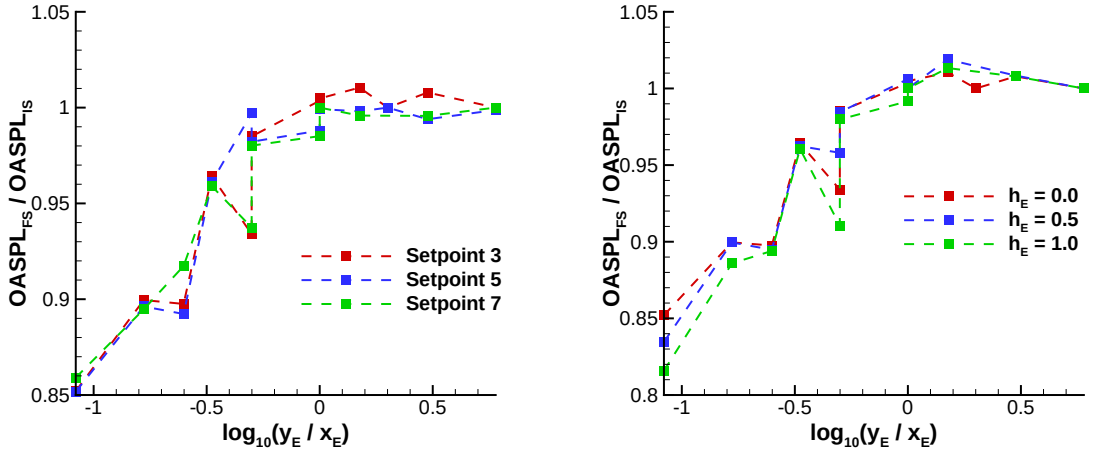

(a) Setpoint Variations (b) h_E Variations

Figure 5. Normalized OASPL for all surface spans (y_E/x_E) acquired at $\theta = 90°$, $\phi = 0°$ as setpoint and standoff distance (h_E) vary.

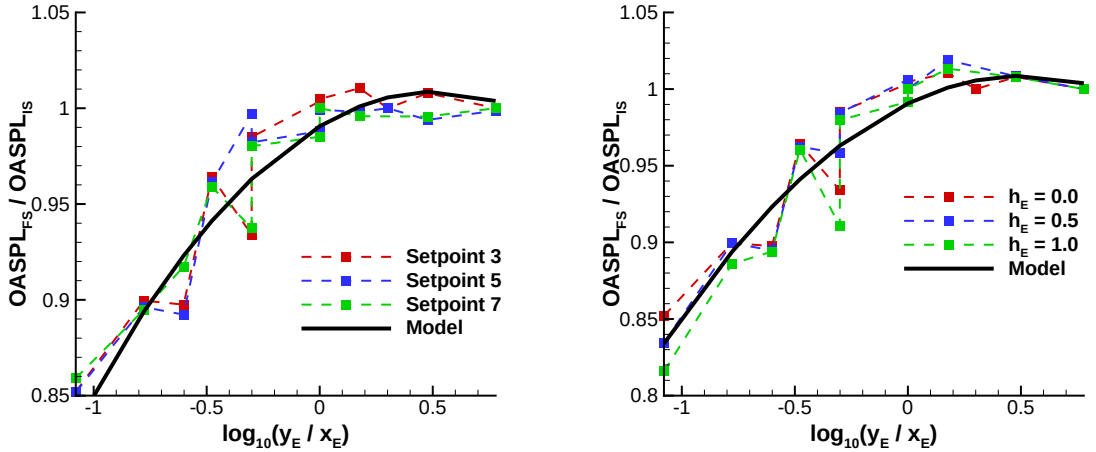

(a) Setpoint Variations (b) h_E Variations

Figure 6. Normalized OASPL data and model results for all surface spans (y_E/x_E) acquired at $\theta = 90°$, $\phi = 0°$ as setpoint and standoff distance (h_E) vary.

(Figures 7(c) and 7(d). The upper frequency range of the JSI noise and lower frequency range of the shielding effect may also overlap making it difficult to determine where the shielding effect begins in the remnants of the coherence-based separation used to extract the JSI noise spectra (e.g. $0.5 < St_{Dj} < 1$ in Figure 7(d)).

The shielding effect model for the infinite span surface was developed by first taking only the negative values from the shielding effect spectra (G_S) and performing a linear fit (in $log_{10}(St_{Dj})$) to reduce the spectral variations.[9] The coefficients from these linear equations were then used to form the model. This process is now used to provide a smooth spectra to develop the finite span shielding effect model. However, instead of fitting the resulting coefficients, the model spectra are numerically integrated (in dB, not power) to give an estimate of shielding effect associated with a finite span at a given observer azimuthal angle. These integrated estimates are then divided by the estimate for the corresponding (x_E, h_E, θ, and ϕ) infinite span surface to give a percentage change in the shielding effect associated with each finite span length. Note that the integration is not an OASPL but integrated dB values so that larger magnitude negative numbers indicate more shielding and, when normalized, larger values represent more shielding. This normalization places natural limits on the model where $C_{span,shield} = 1$ indicates shielding equivalent to the infinite span and $C_{span,shield} = 0$ indicates a complete loss of shielding.

The finite span shielding model modifies the amplitude returned by the infinite span model on a frequency by frequency basis to account for the reduction of surface span length. Mathematically, $C_{span,shield}$ appears in the shielding effect (G_S) model as:

$$G_S = \mathbf{C_{span,shield},}_{\phi}\left[C_{1,S,\theta}\, log_{10}(St_{Dj}) + C_{2,S,\theta}\right] \tag{10}$$

where $C_{span,shield,\phi}$ is a function of surface span (y_E), surface standoff distance (h_E), jet diameter (D_j), and observer azimuthal angle (ϕ). Note that $C_{span,shield,\phi}$ is not a function of frequency but only y_E, h_E, D_j, and ϕ.

The normalized shielding data is shown in Figures 8(a)-8(j). Assuming line of sight propagation of sound and neglecting edge effects, then a line from the jet centerline through the spanwise edge of the surface will divide the shielded observers (lower ϕ) from the unshielded observers. The normalized shielding effect determined from the experimental data are plotted as a function of ϕ_E, the azimuthal angle between the jet centerline and the spanwise edge of the surface in Figures 8(a)-8(j). Mathematically, the angle ϕ_E is defined as:

$$\phi_E = tan^{-1}\left(\frac{y_E/2}{h_E + D_j/2}\right) \tag{11}$$

where $\phi_E = 90^\circ$ represents an infinite span and $\phi_E = 0^\circ$ represents zero span (line surface).

The model coefficients were determined using a linear least-squares fit over the range of data points statistically different from zero. This range was based on normalized experimental shielding data at $\phi = 90^\circ$ (Figure 8(a)); by definition there is no shielding at this observer angle so the mean ($\overline{C_{span,shield,\phi=90}} \approx 0.1$) can be used to represent the unshielded level. The finite span model uses the linear equation:

$$C_{span,shield,\phi} = S_{1,\phi}\phi_E + S_{2,\phi} \tag{12}$$

where $S_{1,\phi}$ and $C_{2,\phi}$ are the linear and constant coefficients respectively determined at each observer azimuthal angle. These coefficient are shown in Table 3. Note that the normalization process established zero and one as the lower and upper limits of the model; these should be enforced when the model is implemented as this linear model is not naturally limited.

The finite span shielding model can be applied by linear interpolation between the nearest azimuthal angles listed in Table 3. Alternatively, Figure 9 shows that these coefficients can be well represented in the range $0 \leq \phi \leq 80^\circ$ by the cubic equations:

$$S_{1,\phi} = 1.2864^{-7}\phi^3 - 9.5491^{-6}\phi^2 + 3.8680^{-4}\phi + 2.7790^{-3} \tag{13}$$

$$S_{2,\phi} = -1.4899^{-5}\phi^3 + 1.1933^{-3}\phi^2 - 4.2593^{-2}\phi + 7.1968^{-1} \tag{14}$$

Interpolation is still required for observer angles $\phi > 80^\circ$ but Equations 13 and 14 can be used for most observer angles.

ϕ	$S_{1,\phi}$	$S_{2,\phi}$
90°	0	0
80°	0.0397	-2.7358
70°	0.0278	-1.4296
60°	0.0201	-0.7192
50°	0.0160	-0.3832
40°	0.0117	-0.0219
30°	0.0108	0.0891
20°	0.0088	0.2021
10°	0.0061	0.5158
0°	0.0041	0.6603

Table 3. Coefficient for the finite span shielding model.

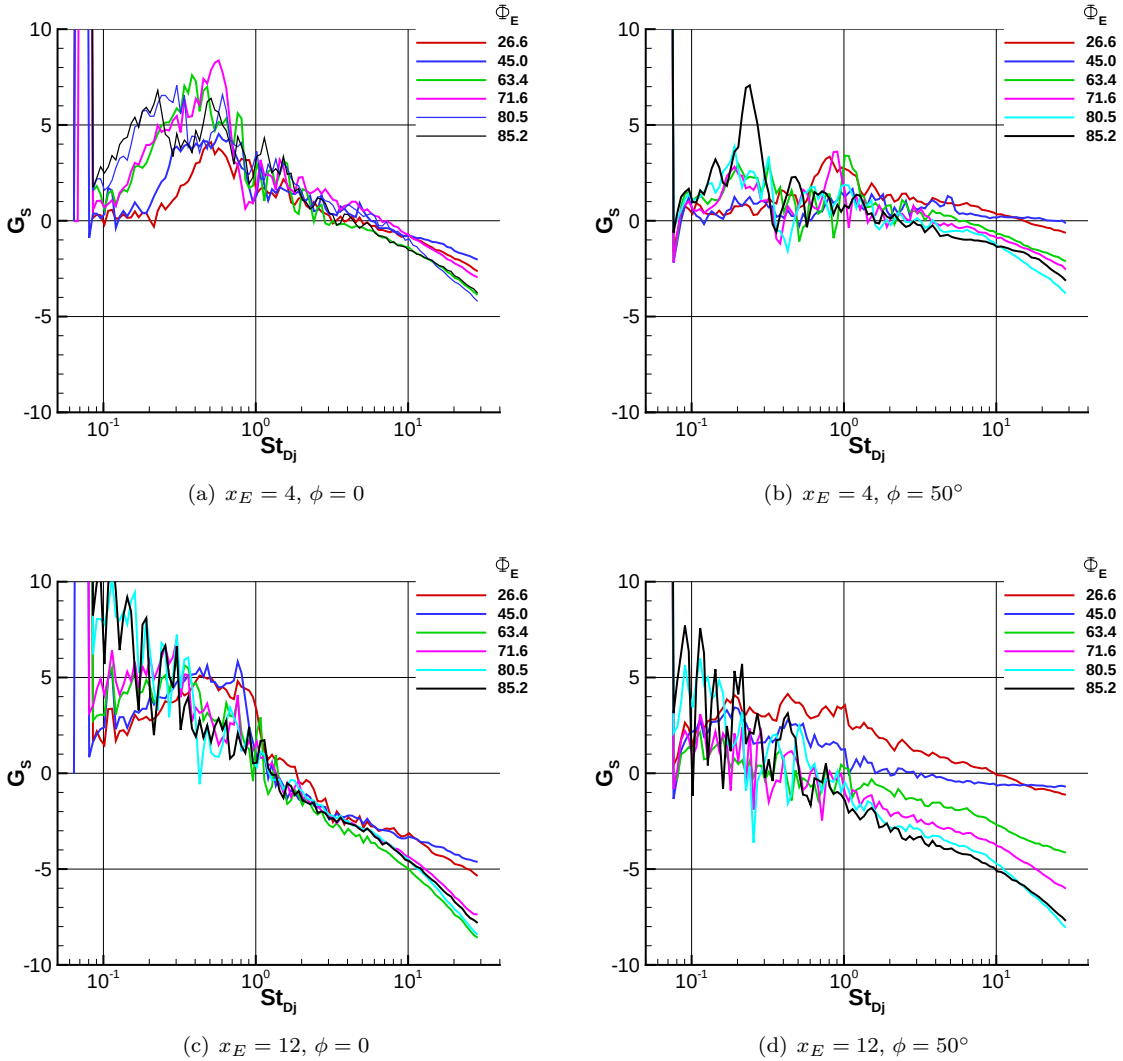

(a) $x_E = 4$, $\phi = 0$

(b) $x_E = 4$, $\phi = 50°$

(c) $x_E = 12$, $\phi = 0$

(d) $x_E = 12$, $\phi = 50°$

Figure 7. Shielding effect (G_S) extracted from the measured data for different surface lengths (x_E) and observer azimuthal angles (ϕ) identified by the angle between the jet centerline and the spanwise edge of the surface (ϕ_E).

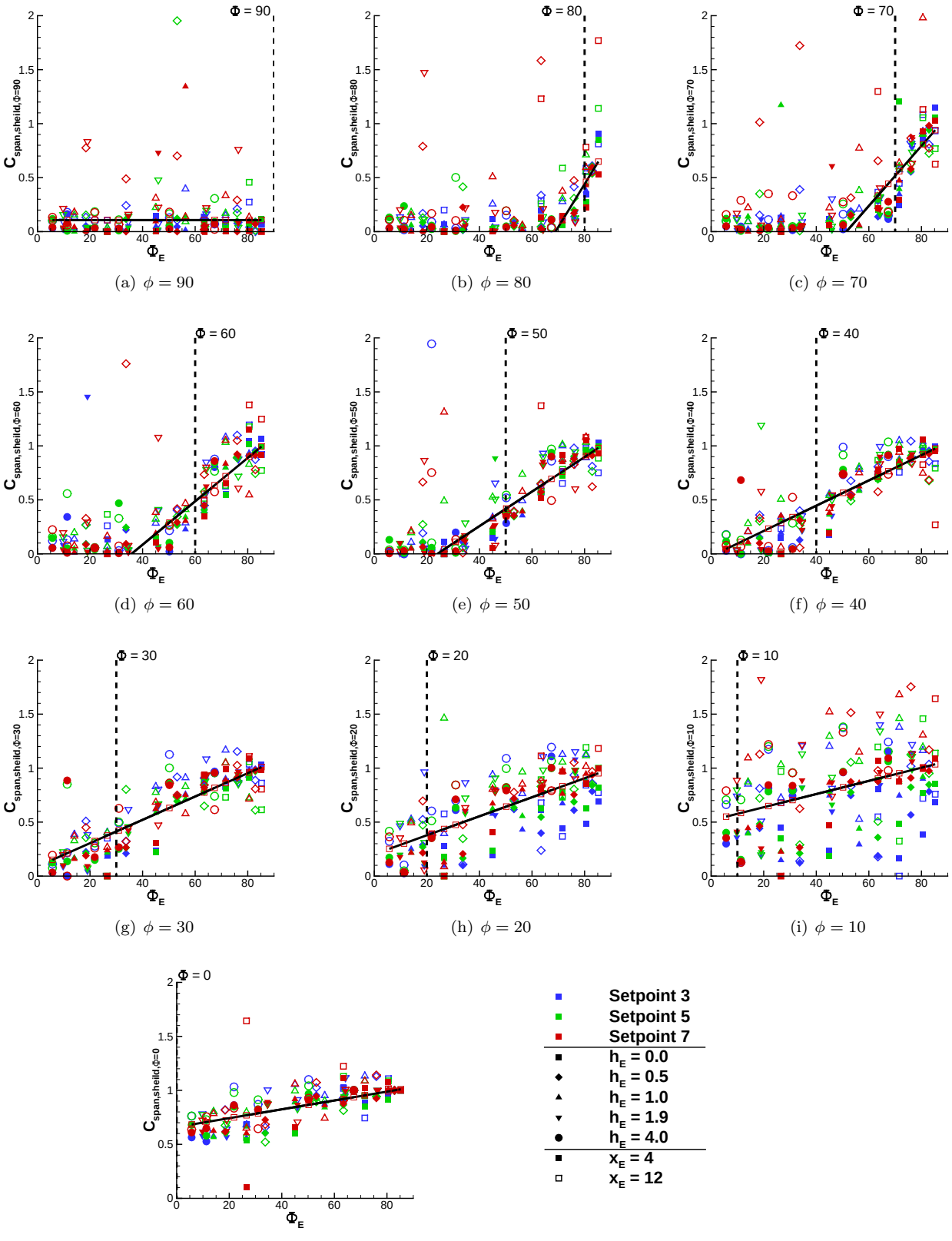

(a) $\phi = 90$ (b) $\phi = 80$ (c) $\phi = 70$

(d) $\phi = 60$ (e) $\phi = 50$ (f) $\phi = 40$

(g) $\phi = 30$ (h) $\phi = 20$ (i) $\phi = 10$

(j) $\phi = 0$ (k) Legend

Figure 8. Shielding coefficients data (red) and model (black) to account for finite span effects with data at each observer azimuthal angle (ϕ, dashed line) as a function of the angle between the jet centerline and the surface edge (ϕ_E).

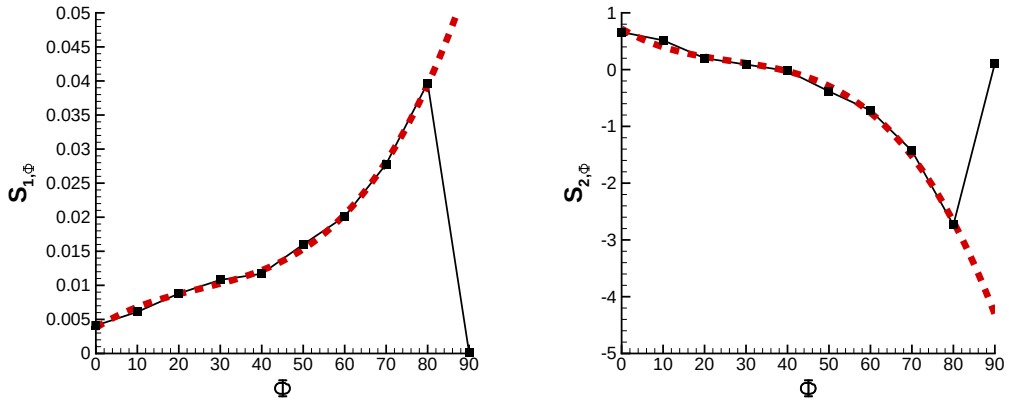

(a) S_1 (b) S_2

Figure 9. Coefficients $S_{1,\phi}$ and $S_{2,\phi}$ plotted as a function of observer azimuthal angle (ϕ) (black) with the fitted cubic functions given in Equations 13 and 14 (red) for $S_{1,\phi}$ and $S_{2,\phi}$ respectively.

III.D. Comparison to Data

The finite span models provide an amplitude adjustment to the noise or shielding effect produced by an infinite span surface. The finite span models, therefore, easily integrate into the overall spectral prediction defined in Equation 3, extending over the range defined by the infinite span models. However, for verification the models are compared to data on the azimuthal and polar arcs used during those experiments. Figure 10 shows a comparison between predicted and measured spectra at setpoint 3, $x_E = 4$, $h_E = 0$, and $y_E = 6$. At this span the JSI span model should return a value of one ($y_E/x_E > 1$) but the span correction on the shielding model should be active; the comparison is reasonable with most areas in the ± 1 range on both the polar and azimuthal arcs indicating that the models are working together as intended. Another example, shown in Figure 11, uses the same jet condition, surface length, and standoff distance but reduces the span to $y_E = 2$ bringing both the JSI span model and the shielding span model into the prediction. Again, the comparison is reasonable indicating that the model and prediction code is working as intended.

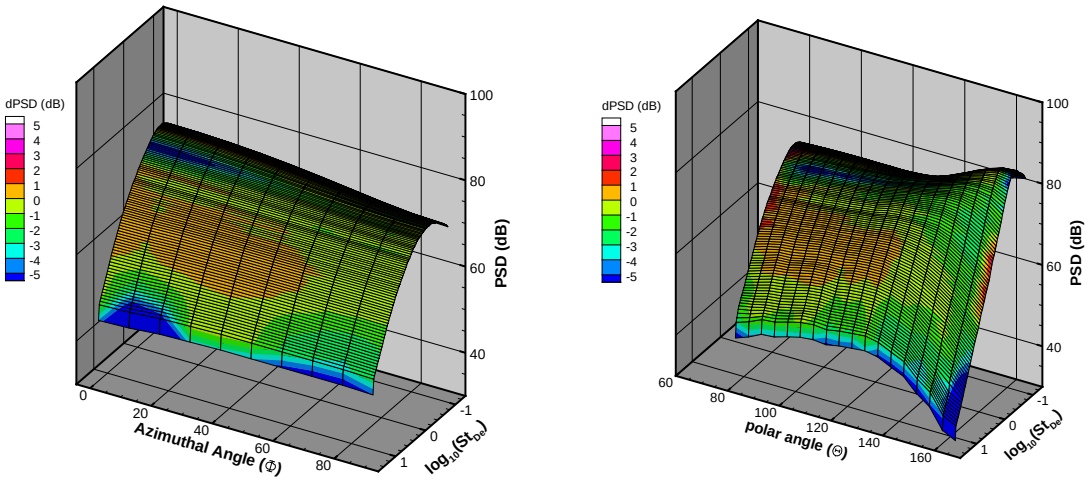

(a) $\theta = 90°$ (b) $\phi = 0°$

Figure 10. Predicted spectra in the azimuthal and polar arcs for setpoint 3, $x_E = 4$, $h_E = 0$, $y_E = 6$ with color contours to indicate the difference to the measured data.

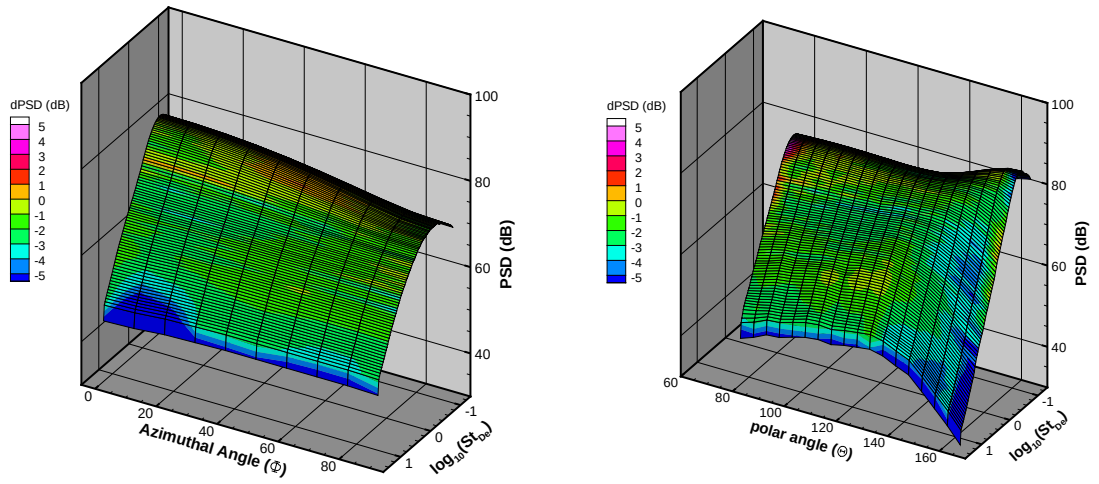

(a) $\theta = 90°$ (b) $\phi = 0°$

Figure 11. Predicted spectra in the azimuthal and polar arcs for setpoint 3, $x_E = 4$, $h_E = 0$, $y_E = 2$ with color contours to indicate the difference to the measured data.

IV. Summary

Far-field experimental noise data have been acquired for a simple single-stream round jet near a flat surface with finite span. These data have been used to build an empirical models that describes the effect of finite span on the jet-surface interaction noise source and the shielding of the jet mixing noise. These models have been integrated into existing models for the JSI noise source and shielding effect developed for semi-infinite surfaces. Both finite span models work by modifying the predictions from the semi-infinite span models to extend their range over observer locations not covered by the underlying experiments. The addition of finite span models in these tools for system level noise prediction adds another element of realism to provide a more accurate assessment of the system level trade-offs involving engine/airframe integrations and the implications to exhaust noise.

Acknowledgements

This work was supported by the NASA Advanced Air Vehicle Program, Advanced Air Transportation Technologies and Commercial Supersonic Transport Projects.

References

[1]Head, R.W. and Fisher, M.J., "Jet/Surface Interaction Noise: Analysis Of Farfield Low Frequency Augmentation of Jet Noise Due To The Presence Of A Solid Surface", AIAA 1976-502, 1976.

[2]Lawrence, J.L.T., Azarpeyvand, M., and Self, R.H., "Interaction between a Flat Plate and a Circular Jet", AIAA 2011-2745, 2011.

[3], Brown, C., "Jet-Surface Interaction Test: Far-Field Noise Results", ASME GT2012-69639, 2012.

[4]Brown, C.A. , "Jet-Surface Interaction Test: Far-Field Noise Results", J. Eng. Gas Turbines Power, **1**35(7), Jun. 2013.

[5]Podboy, G., "Jet-Surface Interaction Test: Phased Array Noise Source Localization Results", ASME GT2012-69801, 2012.

[6]Brown, C. and Bridges, J., "Small Hot Jet Acoustic Rig Validation", NASA/TM-2006-214324, 2006.

[7]Bridges, J. and Brown, C., "Validation of the Small Hot Jet Acoustic Rig for Jet Noise Research", AIAA 2005-2846, 2005.

[8]Brown, C., "An Empirical Jet-Surface Interaction Noise Model with Temperature and Nozzle Aspect Ratio Effects", AIAA 2015-0229, 2015.

[9]Brown, C., "Empirical Models for the Shielding and Reflection of Jet Mixing Noise by a Surface", to be presented at the 2015 AIAA Aviation Conference.

[10]Khavaran, A. and Bridges, J., "Development of jet noise power spectral laws using SHJAR data", AIAA 209-3378, 2009.

[11]Khavaran, A. and Bridges, J., "SHJAR jet noise data and power spectral laws", NASA/TM 2009-215608, 2009.

[12]Brown, C., "Developing an Empirical Model for Jet-Surface Interaction Noise", AIAA 2014-0878, 2014.